DROPLET MANIPULATION ON STRUCTURED SHAPE MEMORY POLYMER SURFACE

BY

JUN KYU PARK

THESIS

Submitted in partial fulfillment of the requirements
for the degree of Master of Science in Mechanical Engineering
in the Graduate College of the
University of Illinois at Urbana-Champaign, 2017

Urbana, Illinois

Advisor:

Assistant Professor Seok Kim

ABSTRACT

While methods for dynamic tuning of surface wettability to manipulate water droplets have been widely explored for many applications including digital microfluidics, those based on dynamically changeable surface morphology have remained challenging to achieve. In this work, we present a structured shape memory polymer (SMP) surface which shows dynamically tunable surface wettability through changeable surface morphology in order to manipulate water droplets. The structured SMP surface involves a SMP pillar array consisting of nanotextured small and large pillars which can change its morphology between permanent and temporary shapes upon thermomechanical loading. Specifically, the structured SMP surface dynamically creates a surface morphological gradient and changes its surface wettability during thermally induced shape recovery of the SMP pillar array. Different wetting characteristics of the structured SMP surface between permanent and temporary shapes are theoretically predicted and experimentally verified. Based on these measured wetting characteristics, the structured SMP surface is designed to demonstrate that the morphological difference between two shapes under a water droplet overcomes contact angle hysteresis, resulting in driving a water droplet, when combined with the thermal Marangoni effect.

ACKNOWLEDGMENTS

First of all, I would like to express the deepest appreciation to my adviser, Seok Kim, for his support and belief on me through the trials and errors. I am extremely fortunate to have got all the support along the assigned work. I respect and thank him for giving me an opportunity to involve in this assignment and providing me a great working environment.

Also thanks to my laboratory members, Hohyun Keum, Jeffrey Eisenhaure, and Zining Yang who trained me and gave me a tip on experiment. This assignment cannot be successfully completed without their effort and help. Last but not least, I am really grateful to my family who endured and supported me financially and emotionally along this long process.

TABLE OF CONTENTS

LIST OF SYMBOLS

CAH	Contact angle hysteresis
SMPs	Shape memory polymer
BOE	Buffered oxide etchant
DRIE	Deep reative ion etch
FDTS	Heptadecafluoro tetra hydrodecyl-trichlorosilane
ITO	Indium tin oxide
TCL	Three phase contact line
a	lateral dimension of large pillar
b	lateral dimension of small pillar
c	lateral dimension of large pillar base
d	lattice size of pillar array
f	Solid fraction
f_{ori}	Solid fraction of original SMP pillar array
f_{def}	Solid fraction of deformed SMP pillar array
f_F	Solid fraction of geometry beneath front of droplet
f_R	Solid fraction of geometry beneath rear of droplet
F_T	Thermal Marangoni force

F_M	Morphological gradient force
F_H	Hysteresis force
F_{tot}	Total driving force
g	Gravitational acceleration constant
h_{men}	Meniscus height of droplet on original SMP pillar array
h_{ori}	Height difference between large and small pillar of original SMP pillar array
h_{def}	Height difference between large and small pillar of deformed SMP pillar array
m	Mass of droplet
N_1	The number of large pillars in repeating lattice
N_2	The number of small pillars in repeating lattice
r	Roughness ratio
r_{ori}	Roughness ratio of original SMP pillar array
r_{def}	Roughness ratio of deformed SMP pillar array
r_f	Roughness ratio of geometry beneath front of droplet
r_r	Roughness ratio of geometry beneath rear of droplet
R	Radius of droplet base
$\mathrm{T_g}$	Glass transition temperature of SMP
θ^*	Apparent contact angle

$\theta^{*}_{\mathrm{ori}}$	Apprent contact angle on original SMP pillar array
$\theta^{*}_{\mathrm{def}}$	Apprent contact angle on deformed SMP pillar array
θ^{*}_{F}	Apprent contact angle of front of droplet
θ^{*}_{R}	Apprent contact angle of rear of droplet
θ^{*}_{m}	Measured apparent contact angle
θ^{*}_{t}	Theoretical apparent contact angle
θ_{Y}	Intrinsic contact angle
$\theta_{a\mathrm{dv}}$	Advancing contact angle
$\theta_{a\mathrm{dv,F}}$	Advancing contact angle of front of droplet
θ_{rec}	Receding contact angle
$\theta_{\mathrm{rec,R}}$	Receding contact angle of rear of droplet
θ_{tilt}	Substrate tilting angle
θ_{crt}	Critical substrate tilting angle
γ	water/air Surface tension

CHAPTER 1

INTRODUCTION

1.1 Droplet manipulation

Droplet manipulation on a surface has found numerous applications including in lab-on-a-chip devices,[1–3] particularly when a programmable droplet motion is desired without requiring bulky instruments. To this end, extensive studies have been done on driving forces to manipulate water droplets.

1.2 Literature review

Above all, electrowetting-on-dielectric (EWOD) has been one of the most advanced droplet manipulation strategies. A droplet can be split, merged, and transported with high reversibility through surface tension control in EWOD devices.[4–9] A voltage signal causes electric charge to accumulate at the solid–liquid interface which results in electrocapillary forces altering surface wettability.[4,8,9] Applying sequential voltage signals on a circuit patterned beneath a dielectric layer, a droplet can be manipulated with unbalanced wettability over a surface.[4,7,8] In addition to electrocapillary forces, alternative driving forces to manipulate droplets are available and they are based on thermal,[10–13] chemical,[13–16] and surface morphological gradients.[17–19] For example, thermal gradients cause surface tension gradients of a water droplet on a surface, creating thermal Marangoni forces[10–13] that may drive a water droplet in a favorable direction. Chemical gradients also causing surface tension gradients of a water droplet are achieved by applying functional groups to a surface with spatially varying densities[14–16] or changing chemical components upon temperature gradients.[13] Surface wettability gradients based on surface morphological gradients have also been demonstrated as driving forces for water droplet manipulation.[17–19] While these driving forces are well available, the manipulation of droplets using those forces is often difficult due to the contact angle hysteresis (CAH) of water droplets. In order to manipulate a droplet on a surface, driving forces should overcome the opposing force caused by CAH. It is widely known that CAH is reduced when droplets are in the Fakir wetting regime,[18,20] particularly on a hierarchically structured surface.[24–27] However, CAH is, in common cases, too high compared with available driving forces to manipulate water droplets. Therefore, highly optimized surface design and fabrication are often required to allow manipulation of water droplets using those forces. Other approaches may be adopted to bypass the requirement and to overcome CAH with external aids such as vibrating a surface where a droplet is placed.[12,19]

1.3 Scope of research

In this work, we present a novel strategy enabling the manipulation of water droplets without external aids by utilizing a surface morphological gradient created on a dynamically shape-changing structured shape memory polymer (SMP) surface in combination with the thermal Marangoni effect. SMPs are a broad range of responsive polymers with properties including a configurational memory of 'permanent shape' that is recovered from a deformed shape, i.e. 'temporary shape,' via external stimuli. Particularly for a thermoresponsive SMP, heating the polymer beyond its glass transition temperature (Tg) causes its dramatic elastic modulus transition from 'glassy state' to 'rubbery state'.[28,29] Due to these unique properties, SMPs have been extensively exploited for many applications including robotics,[30,31] biomedical devices,[32,33] microassembly,[34] dry adhesives,[35,36] and sensors.[37,38] Moreover, recent studies on switchable wettability of a SMP pillar array extended SMPs into tunable wetting surfaces.[39–41] Once SMP pillars are bent in their temporary shape and coated with a metal layer with different thicknesses, the SMP pillars after shape recovery become bent with different angles. By differentiating bending angles, various contact angles of water droplets, water droplet spreading, and directed water droplet shedding on the SMP pillar array are demonstrated.[39–41] While this prior work exhibits the potential utility of SMPs for tunable wetting surfaces, dynamic water droplet manipulation using SMPs has still remained for further exploration. Here, we design and fabricate a structured SMP surface including a nanotextured SMP pillar array with a periodic square lattice where water droplets are manipulated. The structured SMP surface shows dynamically tunable wettability during sequential local heating and shape recovery within the Fakir regime that is favorable for a number of applications such as self-cleaning,[24,25] anti-fouling,[42,43] and droplet manipulation.[20,25] Therefore, the fine control over the motion of a droplet is achieved by surface morphological gradient and thermal Marangoni forces which overcome CAH on the structured SMP surface. It is worthwhile to note that the beginning of the droplet motion in this work is not aided by any other sources to alleviate CAH.

CHAPTER 2

METHODS

2.1 Fabrication of a structured SMP surface

Fabrication steps of the structured SMP surface that consists of small and large pillars are depicted in Fig. 1. It involves polydimethylsiloxane (PDMS) and SMP molding processes, and starts with creating a Si pillar array as an original master. A thermally grown 1 μm thick SiO_2 layer on a 500 μm thick Si substrate is patterned using an image reversal technique with an AZ5214 photoresist and selective SiO_2 etching with buffered oxide etchant (BOE). The large Si pillars are formed using a deep reactive ion etch (DRIE) process (Pegasus STS DRIE) subsequently (Fig. 1a). Following photolithography and the second DRIE process define the small Si pillars. Here, the lithographically patterned photoresist layer and the previously patterned SiO_2 layer are used as masking layers for the second DRIE process. After the second DRIE process (Fig. 1b), the removal of masking layers including the photoresist and SiO_2 by acetone and BOE completes the fabrication of the Si master.

To enable nanotexturing on top surfaces of the Si pillars, a three step black silicon (bSi) process (PlasmaTherm ICP RIE) is performed (Fig. 1c).[44] The process starts with the formation of a thin SiO_2 film with O_2 plasma. The thin SiO_2 film is incompletely etched by CHF_3 plasma to form randomly scattered SiO_2 islands. The islands are used as etch masks for the successive Si etching steps. With the etch masks, nanocones can be formed by selective Si etching with Cl_2 and Ar plasma.

An anti-stick coating layer of heptadecafluorotetrahydro-decyl-trichlorosilane (FDTS) is deposited on the fabricated Si master in a molecular vapor deposition (MVD) chamber to ease successive polymer casting processes. The SMP pillar array is fabricated via two separate casting processes with PDMS and SMP (Fig. 1d and e). PDMS and SMP precursors are fully degassed in a vacuum desiccator before curing in a convection oven. First, a PDMS precursor is poured into the Si master and cured at 60 °C for 120 minutes to form a PDMS mold with small and large holes. Next, a SMP precursor is cast between a flat smooth indium tin oxide (ITO) coated glass slide and the PDMS mold at 100 °C for 120 minutes. To allow spatially selective heating of SMP pillars, a glass slide with patterned ITO heaters is used during the SMP casting step. Lithographical patterning of a photoresist and a subsequent ITO etching with hydrochloric acid create ITO heaters on the glass. In this work, a particular formulation of thermoset SMP referred to as NGDE2 that is previously developed is used.[29] It is worthwhile to note that the nanotexture formed on the Si master via a bSi process is transferred to the SMP pillars but it becomes coarse after the two step casting processes (Fig. 9).

2.2 Dynamic tuning of apparent contact angle

To demonstrate the dynamic tuning of apparent contact angles, a test sample with a built-in heat source is fabricated. An ITO heater on a glass slide is patterned, and the SMP pillar array is cured and shaped between a PDMS mold and the ITO heater in order to heat the SMP pillar array uniformly. Large pillars are axially compressed such that a water droplet can wet both large and small pillars simultaneously when it is placed on the compressed area. The apparent contact angle of a droplet is investigated during heating the SMP pillar array using the ITO heater with 5 W. T_g (～60 °C) is achieved after around five to ten seconds, and the temperature reaches a steady state (～130 °C) after 30 seconds.

2.3 Droplet manipulation on a horizontal surface

To demonstrate a manipulated droplet, an ITO layer on a glass slide is patterned into separate ITO heaters so as to be activated independently (Fig. 5a). The independent ITO heaters are programmable for spatial gradual and local shape recovery of SMP pillars, enabling different local contact angles on the droplet base. Since heat dissipation through the SMP surface is inevitable, the local heating also generates temperature gradients over the SMP surface. Therefore, driving forces to manipulate droplets in this work are not only a morphological gradient force by the local shape recovery of SMP pillars but also a force caused by thermal gradients (Fig. 5a). Individual ITO heaters on a glass are sequentially activated as the rear of a droplet passes the individual heaters in order to apply a continuous driving force on the droplet. Manipulation of a droplet starts with activation of the nearest heater from the rear of a droplet. After the rear-most part of the droplet passes over the next adjacent heater along droplet pathway, the next heater is activated. The same strategy is applied for the following individual ITO heaters.

2.4 Droplet manipulation on tilted surface

The total net force to drive a water droplet is experimentally measured by matching the total net force to the gravitational force on a tilted substrate. The structured SMP surface on an ITO heater patterned glass substrate is placed on a Dual-Axis Goniometer (THORLABS). After a droplet is placed on the deformed SMP surface, the substrate is tilted by rotating the goniometer knob (Fig. 7a). Once the substrate reaches the target tilting angle, an ITO heater located right behind a droplet is activated to move the droplet uphill.

CHAPTER 3

RESULT AND DISCUSSION

3.1 Characteristics of the fabricated structured SMP surface

3.1.1 Wetting characteristics of the SMP and a hydrophobic coating

The SMP used in this work is inherently hydrophilic and has an intrinsic contact angle of 79.6°. However, in order to get a Fakir droplet on the SMP surface, the surface must have an intrinsic contact angle over 90.0°, which is a hydrophobic threshold. To change the surface chemistry, a FDTS hydrophobic coating monolayer is deposited on the SMP surface. The intrinsic contact angle on a FDTS coated smooth and flat SMP surface is measured as 114.7°. It is noteworthy that FDTS coating forms a monolayer on the SMP surface which is not seriously damaged from heat and mechanical loads.[45] Therefore, the FDTS coated SMP surface with small and large pillars can be used repetitively without significant function deterioration.

3.1.2 Permanent and temporary shape of the SMP pillar array with different wetting characteristics

The structured SMP surface is designed such that a water droplet only wets top surfaces of large pillars when the surface is in the permanent shape (Fig. 3). However, when large pillars are in the temporary shape or axially compressed, a water droplet wets not only large pillars but also small pillars. As depicted in Fig. 3c, the theoretically required height difference between large and small pillars (h_{ori}) to ensure non-wetting on small pillars in the permanent shape is larger than the meniscus height (h_{men}) of a water droplet placed on large pillars. Assuming a two dimensional interface of a droplet, the meniscus height can be obtained theoretically as shown in eqn (1).

$$h_{men} = \frac{\sqrt{2}(d-a)}{2}\left[sec(\pi-\theta_Y) - tan(\pi-\theta_Y)\right] \qquad (1)$$

where θ_Y is the intrinsic contact angle of a FDTS coated smooth and flat SMP surface, d is the lattice size of the large pillar array, and a is the lateral dimension of the large pillars. Here $\sqrt{2}(d-a)$ indicates the diagonal distance between corner pillars. Based on pre-determined θ_Y, d, and a, h_{men} is calculated to be 30 µm. Here, h_{ori} is set to be 80 µm, larger than h_{men} in the permanent shape so that a water droplet on an original SMP pillar array only wets large pillars, yet without causing large pillars to be buckled during axial compression. However, in the temporary shape, h_{def} is 20 µm, smaller than h_{men} so that a water droplet wets all deformed large pillars and top surfaces of small pillars (Fig. 3). It is important to note that the threshold h_{ori} value should be higher than h_{men} in real experiments due to the water hammer effect during dispensing a water droplet on the SMP surface.[46]

The apparent contact angle of a water droplet is defined as the contact angle of a water droplet on the structured SMP surface. Theoretically, the apparent contact angle (θ^*) is calculated from the intrinsic contact angle (θ_Y) and geometric parameters such as the solid fraction and roughness ratio of a surface. In the Fakir wetting regime, a water droplet sits on top of pillars and air pockets (Fig. 3c). Therefore, the projected area of a droplet base becomes a heterogeneous surface with the wetted solid area and the area of air. The portion of the wetted solid area divided by the projected area is the solid fraction (f). On the other hand, the roughness ratio (r) is the ratio between the actual wetted surface area and the projected wetted area. In this work, a water droplet is assumed to wet the nanotexture on the SMP surface completely. The apparent contact angle is derived from the surface tension balance and it is shown in eqn (2).[47]

$$\cos\theta^* = r \cdot f \cdot \cos\theta_Y + f - 1 \tag{2}$$

In a repeating lattice, there are N_1 large pillars and N_2 small pillars (Fig. 3d). The large and small square pillars have the lateral dimensions of a and b, respectively. Because of the axial compression, the height of the large pillars is reduced to h_{def}, and the lateral dimension of the large pillar base (c) becomes larger due to the Poisson effect as depicted in Fig. 2b. The solid fraction of original and deformed SMP pillar arrays, f_{ori} and f_{def}, respectively, is written as eqn (3) and (4).

$$f_{ori} = \frac{N_1 \cdot a^2}{d^2} \tag{3}$$

$$f_{def} = \frac{N_1 \cdot c^2 + N_2 \cdot b^2}{d^2} \tag{4}$$

The roughness ratio on the original pillar array (r_{ori}) originating from the nanotexture is calculated by equating the measured apparent contact angle on the original pillar array (θ^*_{ori}) and θ_Y as shown in eqn (5). The roughness ratio from the nano-texture is also assumed to be uniform throughout the surface, which is verified by investigating the SEM images.

$$r_{ori} = \frac{[(\cos\theta^*{}_{ori} + 1)/f_{ori} - 1]}{\cos\theta_Y} \tag{5}$$

In addition, the sidewall of compressed large pillars is assumed vertical and smooth since bSi is not formed on sidewalls but only on top surfaces due to the vertical etching nature of the bSi process. On deformed large pillars, a water droplet also wets the sidewalls of the large pillars. This creates another fraction of roughness in addition to that from the nanotexture, which is shown in eqn (6).

$$r_{def} = r_{ori} + \frac{4 \cdot N_1 \cdot a \cdot h_{def}}{N_1 \cdot c^2 + N_2 \cdot b^2} \tag{6}$$

From the SEM images (Fig. 2b), the dimensions of pillars are measured and the theoretical apparent contact angles are calculated using eqn (2)–(6), accordingly. Table 1 summarizes all measured and calculated parameters. The detailed calculation procedure is described in the supporting information.

3.2 Dynamic tuning of apparent contact angle

The apparent contact angle significantly increases after shape recovery of the nanotextured SMP pillar array upon uniform heating. It was experimentally observed that a water droplet gradually loses its contact with small pillars, resulting in the gradual reduction of the solid fraction of the SMP surface and the increasing apparent contact angle of the droplet. This means that the water droplet becomes the Fakir droplet that exclusively wets large pillars. Interestingly, when the nanotextured SMP pillar array is only heated up to T_g, the dynamic increase in the apparent contact angle is negligible. This shows that the shape recovery of the SMP large pillars is not the sole reason for the significant increase in the apparent contact angle. From this aspect, the dynamic tuning of apparent contact angles is presumably achieved not only by shape recovery of the SMP surface but also by thermal energy input although further investigation remains for future work. It is worthwhile to note that a similar observation has been pointed out previously. Adera achieved a Fakir droplet on a superhydrophilic structured surface aided by a thermal energy input. His observation is supported by the fact that partial water evaporation at the droplet base creates vapor pressure against the complete wetting.[48]

Furthermore, Liu showed a Wenzel to Fakir droplet transition by heating a Wenzel droplet up to the reduced Leidenfrost point.[49] del Cerro also demonstrated that a microstructured surface could facilitate the same transition by further lowering the reduced Leidenfrost point.[50]

The effect of the nanotexture of SMP pillars on the dynamic tuning of apparent contact angles is evaluated by comparing the dynamic transition results using both smooth and nanotextured SMP pillar array samples. On the smooth sample, the apparent contact angle of a water droplet after shape recovery of SMP pillars slightly increases but fails to reach the value measured on the smooth original SMP pillar array ($\theta^* = 158.2°$ in Table 1) as depicted in Fig. 4c. On the other hand, the complete dynamic transition of a water droplet with an almost 20° contact angle change is achieved on the nanotextured sample, and the transition is more gradual compared to that for the smooth sample. These results indicate that the nanotexture has a positive influence on the dynamic tuning of apparent contact angles by lowering the required thermal energy input for the complete transition, which agrees with del Cerro's results.[50]

3.3 Droplet manipulation on horizontal surface

The surface tension between water and air depends on the temperature of a water droplet, and thus the surface temperature gradient creates the surface tension gradient on the droplet base. Internal water flow, also called Marangoni flow, is induced inside the water droplet due to the surface tension gradient. Thermal Marangoni force is a force driven from the flow that causes a droplet to move forward and the magnitude of thermal Marangoni force is expressed in eqn (7). R is the radius of droplet base, γ is water/air surface tension, and x is displacement in parallel with temperature gradient.[10,11,13]

$$F_T = \pi \cdot R^2 \frac{d\gamma}{dx} \qquad (7)$$

In the meantime, by well controlled local heating of the deformed structured SMP surface, a liquid droplet can be placed on the SMP pillar array such that the rear of the droplet is on the shape-recovered pillars while the front of the droplet is still on the deformed pillars. The different solid fraction and apparent contact angles between the rear and front of the water droplet cause the imbalance of Laplace pressure inside the droplet. In case that the rear of droplet has a larger apparent contact angle, the unbalanced pressure generates a force to move the water droplet forward. The amount of the force from this morphological gradient causing the unbalanced pressure is written in eqn (8). θ^*_F and θ^*_R are the apparent contact angles of a droplet at the front and rear.[13,16,17,19]

$$F_M = \pi \cdot R \cdot \gamma \left| cos\theta^*{}_R - cos\theta^*{}_F \right| \qquad (8)$$

There is the third force, i.e., hysteresis force, involved in the interaction between a droplet and the SMP pillar array and it is a major resistance against droplet manipulation. To model the hysteresis force, an advancing contact angle is defined as the maximum contact angle before three phase contact line (TCL) advancing while a receding contact angle is the minimum contact angle before TCL receding. CAH is the difference between advancing and receding contact angles, and a hysteresis force is the pinning force defined via CAH. Since a droplet experiencing a morphological gradient sits on the deformed SMP pillars and intact SMP pillars simultaneously with different wettability, the hysteresis force is defined as the sum of front and rear pinning forces as shown in eqn (9).[16,17,18,20]

$$F_H = \pi \cdot R \cdot \left(r_F \cdot f_F \cdot \left| cos\theta^*{}_F - cos\theta_{adv,F} \right| + r_R \cdot f_R \cdot \left| cos\theta_{rec,R} - cos\theta^*{}_R \right| \right) \qquad (9)$$

r_F and r_R are roughness ratios of SMP pillar surfaces beneath the front and rear of a water droplet. f_F and f_R are solid fractions of the SMP pillar array beneath the front and rear of a water droplet, respectively. $\theta_{adv,F}$ and $\theta_{rec,R}$ are advancing and receding contact angles at the front and rear of a droplet. Therefore, the first two and second two terms of eqn (9) represent the pinning forces at the front and rear of a droplet, respectively. The CAH on intact and deformed nanotextured SMP pillar arrays is measured by the tilting-plate method.[21,23] The CAH on a flat SMP surface is also measured using the sessile drop method.[22,23] Table 2 summarizes the CAH values. As expected, a FDTS coated flat SMP surface is highly adhesive. Furthermore, even on the nanotextured pillar array, CAH is not as small as those for hierarchical structures shown in prior studies presumably due to lower roughness ratio of the nanotextured pillar array.[24-27]

The total net force applied to a droplet is calculated by adding those three involved forces as shown in eqn (10).

$$F_{tot} = F_T + F_M - F_H \qquad (10)$$

If the total net force (Ftot) is greater than zero a droplet moves. However, if it is equal to or smaller than zero, a droplet does not move. It is noted that eqn (7), (8), (9), and (10) are valid only at the onset of droplet motion and not necessarily valid during droplet motion. Therefore, the balance between those three forces provides an indication of whether the structured SMP surface can initiate the motion of a droplet or not. Here, geometric and wettability parameters at the rear of a droplet, θ^*_R, $\theta_{rec,R}$, r_R, f_R, are assumed to equal the measured values on an intact SMP pillar array, θ^*_{ori}, $\theta_{rec,ori}$, r_{ori}, f_{ori}, respectively. Also it is assumed that those at the front of a droplet, θ^*_F, $\theta_{adv,F}$, r_F, f_F, are equivalent to the measured values on a deformed SMP pillar array, θ^*_{def}, $\theta_{adv,def}$, r_{def}, f_{def}, respectively (Table 1. & 2.).

Fig. 5b shows a series of still frames of a manipulated water droplet with thermal Marangoni and morphological gradient forces. The motion can be characterized as repetitive spreading and shrinking of a droplet. When a droplet undergoes the morphological gradient and the thermal Marangoni effect, the shape of droplet is altered to balance the forces by decreasing the rear apparent contact angle and increasing the front contact apparent angle. Once the front apparent contact angle exceeds the front advancing contact angle, the droplet moves forward, however, the rear of a droplet is still pinned, which causes spreading of a droplet. After a droplet spreads, the rear apparent contact angle becomes smaller than the rear receding contact angle. At this moment, a droplet begins to shrink and the rear of droplet shows stick and slip motion. It is observed that the droplet spreading occurs ahead of the droplet shrinking. This is because the rear pinning force is larger than the front pinning force of a water droplet on the structured SMP surface.

To study the influence of the surface morphological gradient force on droplet manipulation compared to that of thermal Marangoni force on it, three control experiments are performed. The first control experiment is done on a flat and smooth SMP surface coated with FDTS. The same amount of temperature gradient is formed over a sample surface with pre-dispensed droplet ($R \approx 3$ mm). However, no meaningful droplet motion is observed. This result shows that thermal Marangoni force induced by the given temperature gradient cannot overcome hysteresis force to drive a water droplet ($R \approx 3$ mm) on flat SMP surface. Unlike droplet manipulation on flat hydrophilic surface,[10] droplet manipulation on hydrophobic surface is often challenging because droplet base radius becomes significantly small on a hydrophobic surface compared to a hydrophilic surface.

The second control experiment is done on an intact SMP pillar array and the same amount of temperature gradient is given over a sample surface with pre-dispensed droplet. The result demonstrates that the thermal Marangoni force is not sufficiently high to overcome the hysteresis force to move a droplet ($R \approx 3$ mm) on the structured SMP surface although the CAH on the intact SMP pillar array is even lower. Therefore, the morphological gradient is regarded to play a key role in overcoming the CAH for this range of droplet size. It is worthwhile to note that a large droplet may move solely by thermal Marangoni force (F_T) without the morphological gradient force (F_M) since F_T is a quadratic function of R but FM and FH are linear functions of R as shown in eqn (7), (8), (9). The theoretically calculated total net forces (F_{tot}) on deformed and intact SMP pillar arrays versus the radius of droplet base are plotted in Fig 6. According to the plot, a droplet can move only with F_T on an intact SMP pillar array if the radius of droplet base increases further ($R > 3$ mm), which is also experimentally observed (Fig. 6).

The third control experiment is done on a SMP pillar array with pre-defined surface morphological gradient (Fig. 7). To prepare this sample, a SMP pillar array is deformed and a part of the deformed area is recovered with localized heating and subsequent cooling. A droplet is then dispensed on the SMP pillar array in the region between shape deformed area and shape recovered area (Fig. 7a). After the droplet resides on the surface, it is observed that the left part of droplet only wets top surface of large pillars in shape recovered area but the right part of droplet wets both large and small pillars in shape deformed area (Fig. 7c and d). This heterogeneous wetting creates morphological gradient force and propels the droplet to the right. Even after the droplet loses the surface morphological gradient, droplet moves further with inertia (Fig. 7e and f). However, when the droplet loses the kinetic energy due to hysteresis force, the droplet becomes stationary (Fig. 7g).

3.4 Droplet manipulation on tilted surface

The total net force to manipulate a water droplet is experimentally measured by matching the total net force to a gravitational force on a tilted substrate. The structured SMP surface on an ITO heater patterned glass substrate is placed on Dual-Axis Goniometer (THORLABS). After a droplet is placed on the deformed SMP surface, the substrate is tilted by rotating the goniometer knob (Fig. 8a). Once the substrate reaches a target tilting angle, an ITO heater located right behind of droplet is activated to move the droplet uphill to observe the initiation of droplet manipulation. A critical tilting angle (θ_{crt}) is defined as the lowest tilting angle on which the droplet does not move since gravitational force equals the total net force. At the threshold tilting angle the total net force and the gravitational force are related as shown in eqn (11).

$$F_{tot} = mg \sin \theta_{crt} \tag{11}$$

The theoretical value of θ_{crt} is calculated as 2.6° based on eqn (7-11) and Table 2. The experimentally measured θ_{crt} lies around 3.5°, which substantiates the validity of theoretical calculations to a great extent (Fig. 8b).

CHAPTER 4

CONCLUSIONS

In conclusion, dynamically tunable wetting characteristics of a structured SMP surface are studied in this work. The surface includes nanotextured small and large SMP pillars that can be deformed by axial compression to exhibit different surface wettability. Different contact angles of a water droplet on the structured SMP surface in an intact permanent shape and in a deformed temporary shape are theoretically predicted and experimentally verified. The structured SMP surface is designed such that the morphological difference between two shapes under the droplet base overcomes contact angle hysteresis to manipulate a water droplet, when combined with the thermal Marangoni effect. Theoretically calculated total net forces to cause the onset of droplet manipulation are experimentally verified by investigating the motion of a droplet on a tilted substrate. This work opens up a new strategy of extending shape memory polymers into further applications requiring dynamic surface wettability tuning and droplet manipulation.

.

CHAPTER 5

FIGURES AND TABLES

Figure 1.

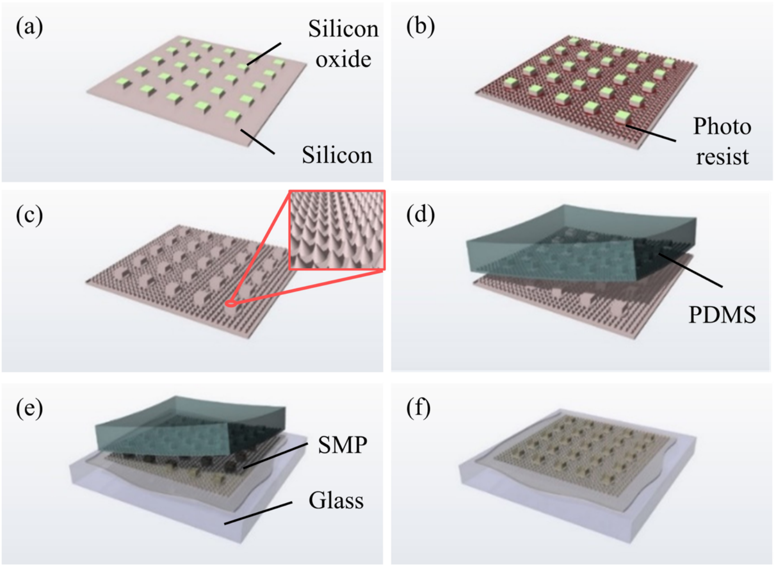

Fig 1. Fabrication flow of a structured SMP surface. (a) A large Si pillar array is formed on a Si substrate by DRIE with a SiO_2 masking layer. (b) A subsequent DRIE with a photoresist masking layer patterns small Si pillars between large pillars. (c) After removing masking layers, the top Si surfaces are nanotextured via a black silicon (bSi) process. (d) A PDMS negative mold is casted. (e, f) A final structured SMP surface on a glass substrate is casted with the PDMS negative mold.

Figure 2.

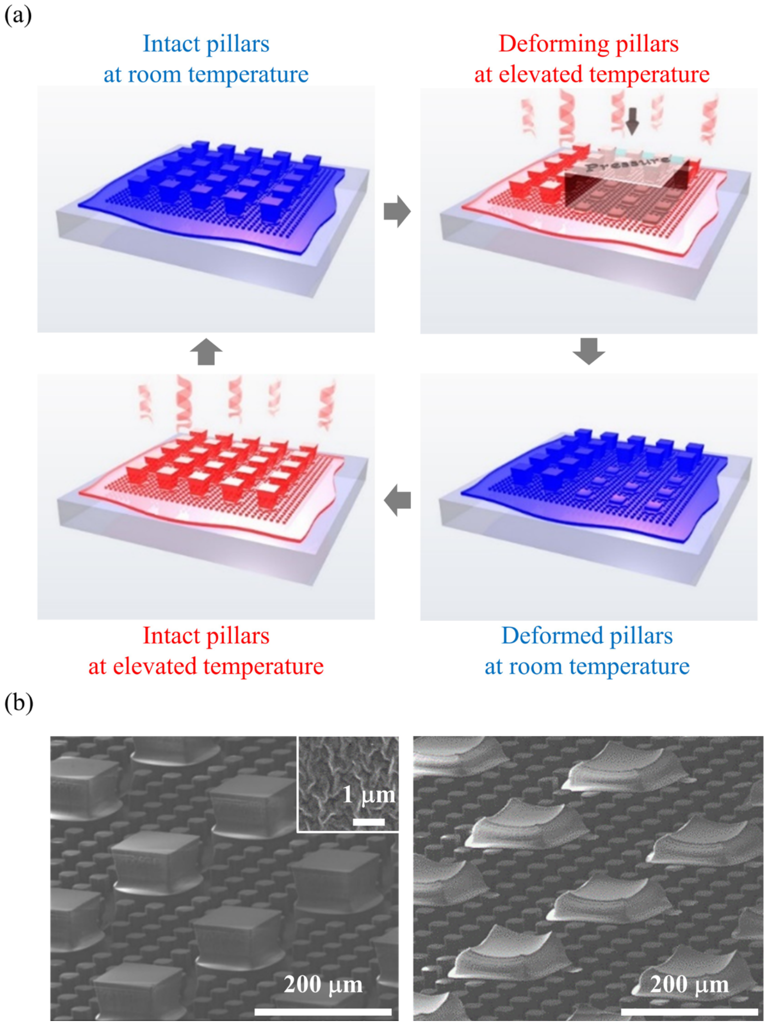

Fig. 2 Intact permanent-shape and deformed temporary-shape SMP pillar arrays. (a) Schematic illustration of a cycle of temporary shape fixing by axial compression under heating and permanent shape recovery by heating. (b) SEM images of the permanent shape (left) and temporary shape (right) of the SMP pillar array. An inset SEM image highlights the nanotexture on SMP pillars.

Figure 3.

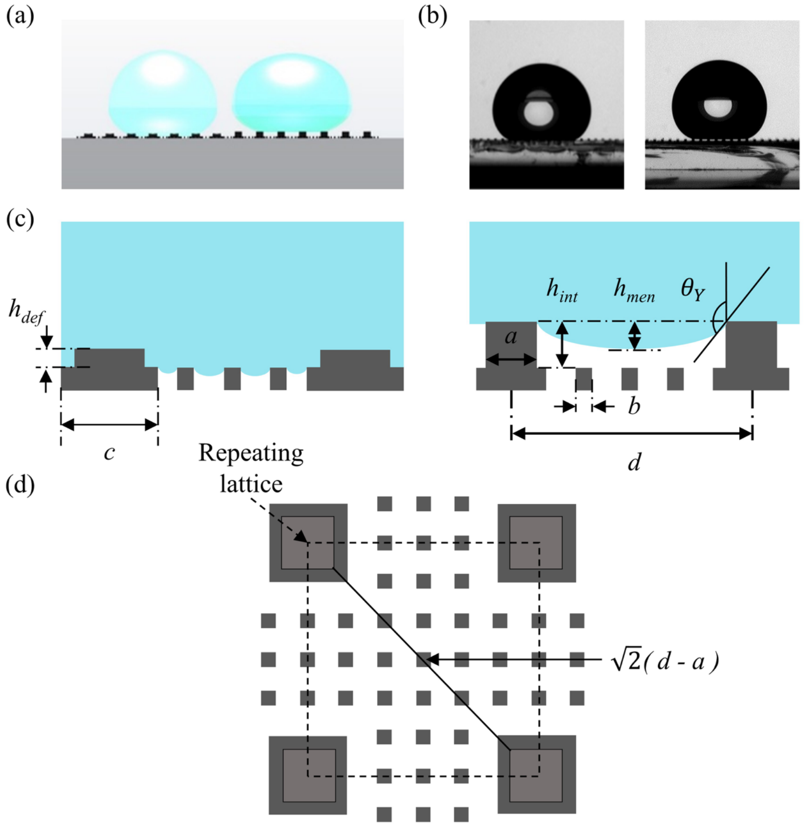

Fig. 3 Two different Fakir droplets on a SMP pillar array. (a) A cartoon illustration comparing different wettings on deformed (left) and intact (right) SMP pillars. (b) Optical images of a water droplet on deformed (left) and intact (right) pillars. Top surfaces of pillars are nanotextured. (c) The dimension of deformed (left) and intact (right) pillars. (d) The schematics of repeating lattice, diagonal line depicts corner pillars

Figure 4.

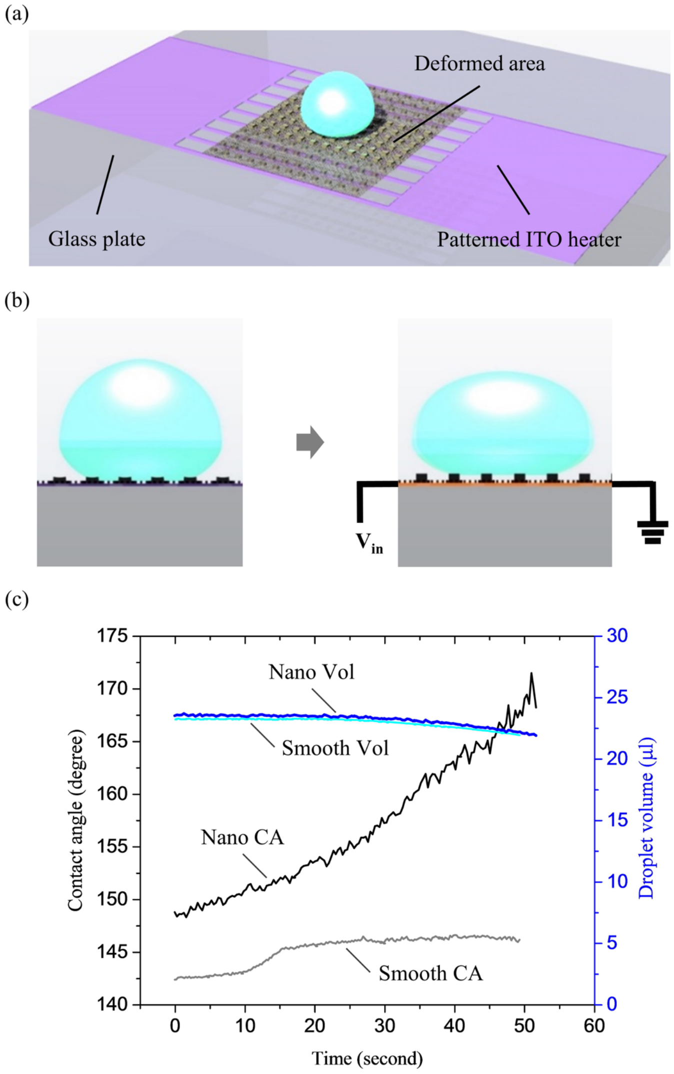

Fig. 4 Dynamic tuning of apparent contact angles. (a) Schematic illustrations of the experimental scheme. A droplet is placed on a deformed SMP pillar array that is formed on an ITO heater. (b) Wetting condition changes of a droplet between on a deformed SMP pillar array (left) and on recovered SMP pillar array upon heating (right). (c) Experimentally measured apparent contact angles and volume changes as functions of heating time for a water droplet on smooth and nanotextured SMP pillar arrays

Figure 5.

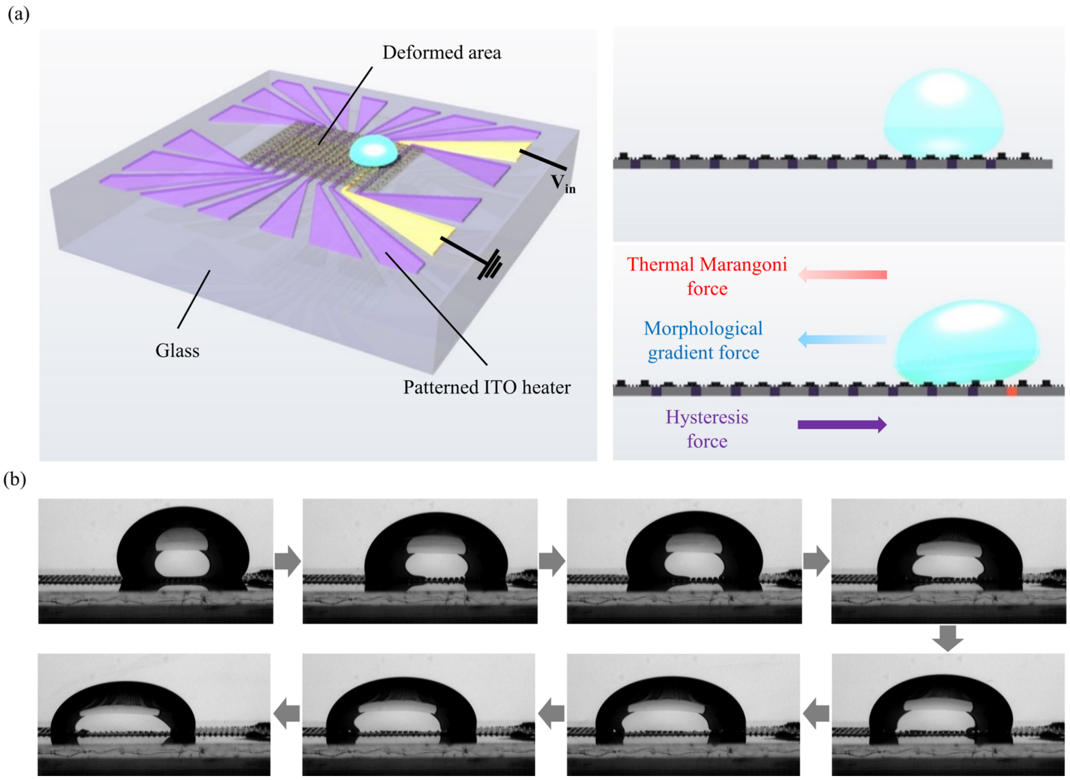

Fig. 5 Manipulation of a droplet on a deformed SMP pillar array with thermal Marangoni and morphological gradient forces. (a) A schematic diagram illustrating a manipulated droplet. A droplet is placed on a deformed SMP pillar array and individually operating ITO heaters beneath it. An operating ITO heater is in yellow and connected with a power source. (left) Side view of the schematic diagram. (right) Upper cartoon depicts a droplet on a deformed SMP pillar array that is ready to move and lower cartoon illustrates the initiation of droplet motion with an activated ITO heater and associated driving forces. (b) Still frames of a manipulated water droplet on the SMP pillar array arranged in time sequence.

Figure 6.

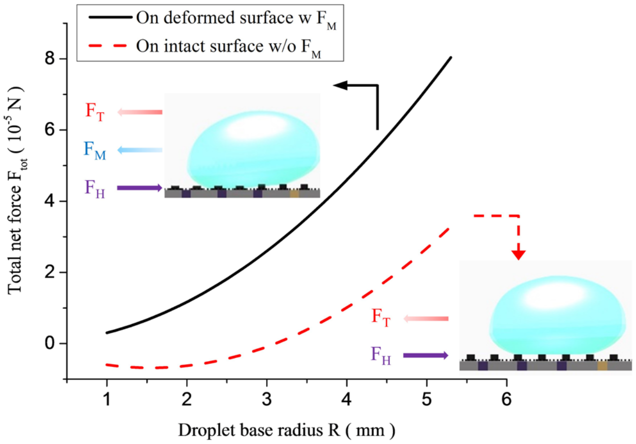

Fig. 6 Plot of the total net force for droplet manipulation on deformed and intact SMP pillar arrays. Upper solid curve in the plot indicates the total net force on a deformed SMP pillar array aided by thermal Marangoni force (F_T) and morphological gradient force (F_M) but with higher hysteresis force (F_H) than that of the intact surface. Lower dotted curve in the plot shows the total net force on an intact SMP pillar array aided only by thermal Marangoni force (F_T) but with lower hysteresis force (F_H) than that of the deformed surface. Lower curve indicates that a droplet cannot be actuated if droplet base radius is smaller than 3 mm.

Figure 7.

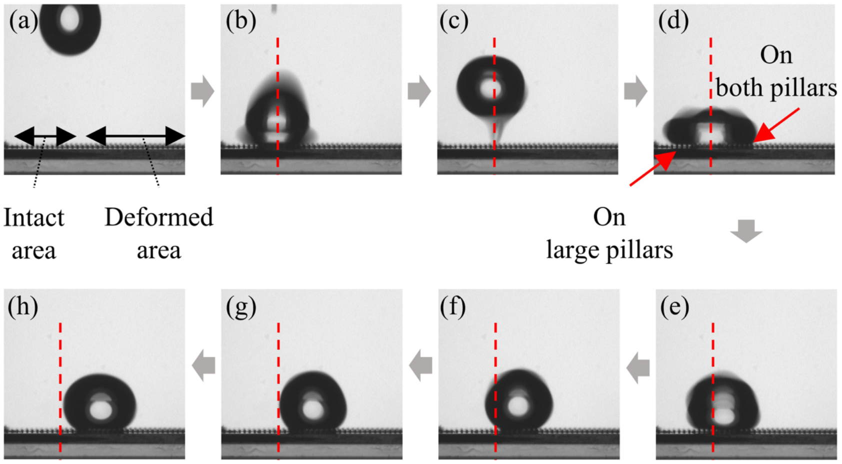

Fig. 7 Series of still images of dispensed droplet on a SMP pillar array with surface morphological gradient in time sequence (a to h). The center of impact is indicated with red dot line to visualize droplet propulsion. (a) Dispending a droplet, (b) First impact of the droplet, (c) Bounce of the droplet, (d) Second impact of droplet, (e) Manipulation of the droplet with surface morphological gradient, (f,g) Travel of the droplet over deformed SMP pillar array, (h) End of droplet movement.

Figure 8.

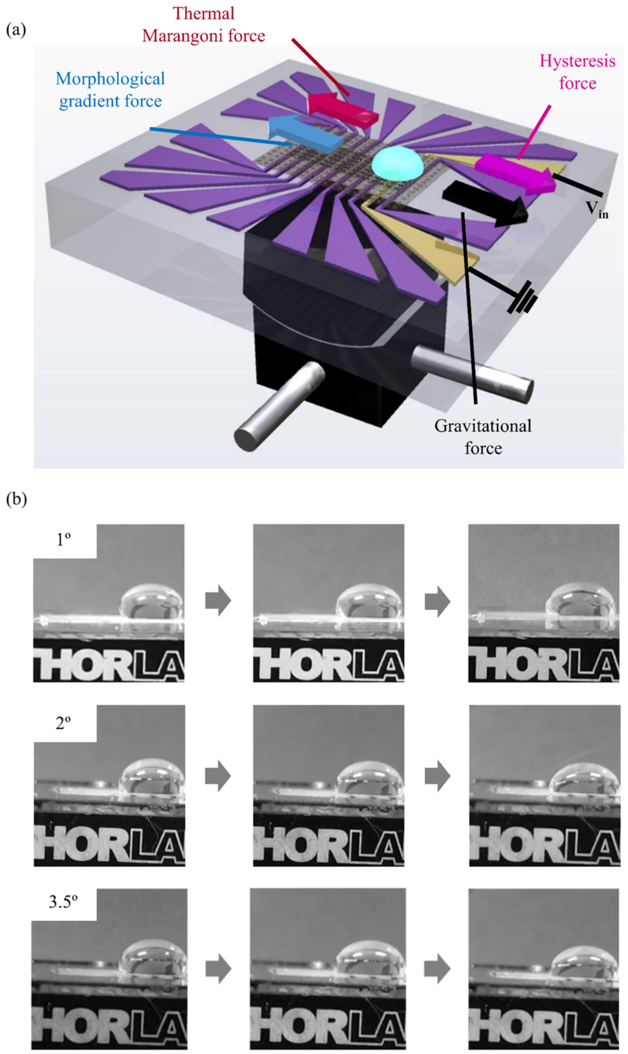

Fig. 8 Droplet motion on a tilted substrate (a) A schematic diagram illustrates the experiment setup. A sample substrate is placed on a goniometer. A droplet is subjected to additional gravitational force against to droplet manipulation. (b) Images of a droplet in time sequence. From droplet manipulation on 1° tilted substrate to barely manipulated droplet on a 3.5° tilted substrate.

Table 1.

Table 1. A summary of solid fraction (f), roughness ratio (r), and apparent contact angles (measured and theoretical, θ*) of intact and deformed SMP pillar arrays with and without nanotexturing. (* For nano-textured intact surface theoretical value is matched to measured one to acquire roughness value of nano-texture using equation (5).)

Surface	State	f	r	Measured θ^*	Theoretical θ^*
Smooth	Original	0.10	1.00	158°	160.63°
	Deformed	0.46	1.19	141°	139.42°
Nano-textured	Original	0.10	1.58	165°	165.00°
	Deformed	0.46	1.76	148°	150.35°

Table 2.

Table 2. Advancing and receding contact angles and corresponding con-tact angle hysteresis of a water droplet on a flat SMP surface, an original SMP pillar array, and a deformed SMP pillar array. All SMP pillar arrays are nanotextured and all samples are FDTS coated

	θ_{adv}	θ_{rec}	CAH
Flat surface	115.9°	33.7°	82.2°
Original pillar array	175.5°	138.7°	36.8°
Deformed pillar array	162.1°	100.5°	61.6°

CHAPTER 6

SUPPORTING INFORMATION

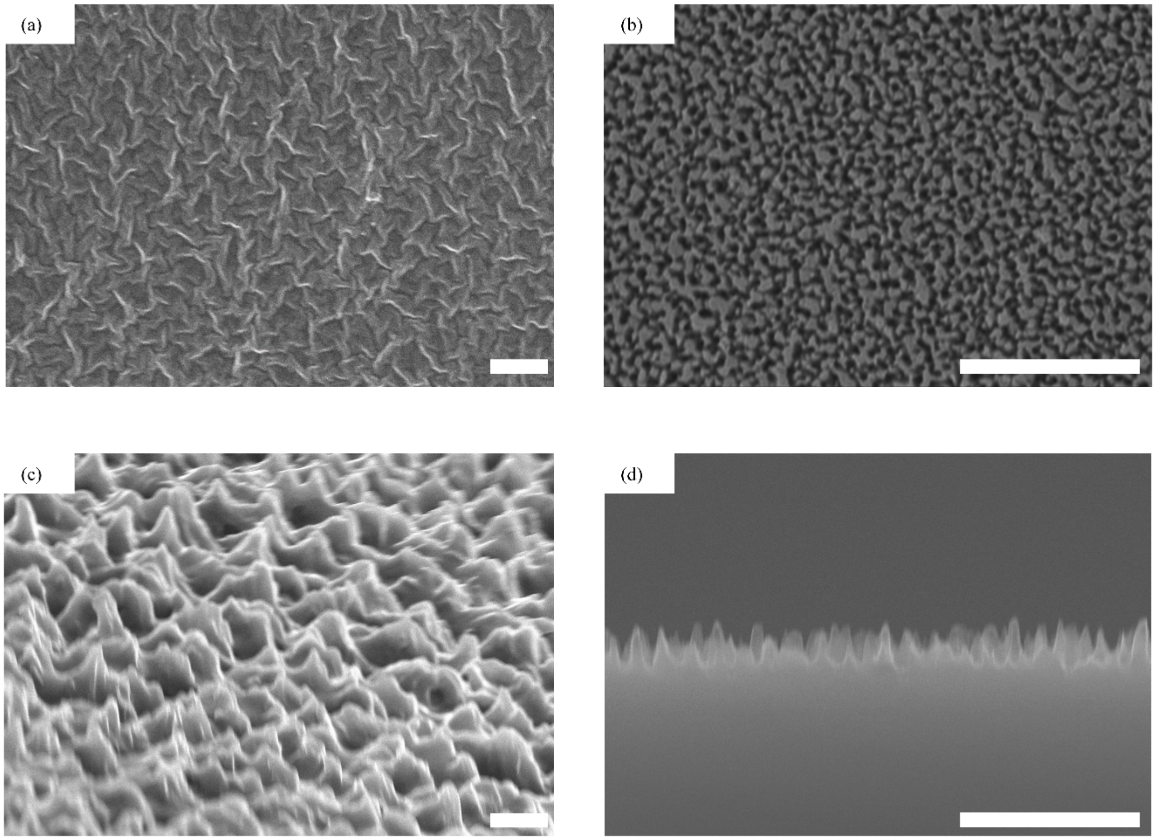

Fig 9. SEM images of nanostructures on SMP pillar array and Si master. White scale bars indicate 1 µm (a) Nanostructure on SMP pillar array (top view), (b) Nanostructure on Si master (top view), (c) 60^o tilted view of Nanostructure on SMP pillar array, (d) Side view of Nanostructure on Si master

Step by step calculation of values in Table. 1

Used values in calculations

- **Geometric values :** *N_1, N_2, a, b, c, and d*

N_1	N_2	**a**	**b**	**c**	**d**
1	*27*	*96.82 μm*	*24.84 μm*	*158.60 μm*	*300.00 μm*

- **Measured values :** Apparent contact angle on nanotextured original pillar array, θ_{ori}^*

1. Calculating solid fractions.

On original structure

$$f_{ori} = \frac{N_1 \cdot a^2}{d^2} = 0.10$$

On deform structure

$$f_{def} = \frac{N_1 \cdot c^2 + N_2 \cdot b^2}{d^2} = 0.46$$

2. Calculating roughness ratio.

Smooth texture ; for droplet on smooth original pillar array, roughness ratio is considered as 1

$$r_{ori} = 1$$

$$r_{def} = r_{ori} + \frac{4 \cdot N_1 \cdot a \cdot h_{def}}{N_1 \cdot c^2 + N_2 \cdot b^2} = 0.19$$

Nano-texture ; roughness ratio from nano-texture, r_{ori}, is back-calculated from the measured apparent contact angle on nano-textured original pillar array.

$$r_{ori} = \frac{\left[\left(\cos\theta_{ori}^* + 1\right)/f_{ori} - 1\right]}{\cos\theta_Y} = 1.58$$

$$r_{def} = r_{ori} + \frac{4 \cdot N_1 \cdot a \cdot h_{def}}{N_1 \cdot c^2 + N_2 \cdot b^2} = 1.77$$

3. Calculating theoretical apparent contact angles

With Smooth texture ; values of r_{ori} and r_{def} are used those of smooth texture.

- **On original structure**

$$\cos\theta^* = r_{ori} \cdot f_{ori} \cdot \cos\theta_Y + f_{ori} - 1 = 160.8°$$

- **On deformed structure**

$$\cos\theta^* = r_{def} \cdot f_{def} \cdot \cos\theta_Y + f_{def} - 1 = 140.0°$$

With Nano-texture ; no calculation is done for the apparent contact angles on nano-textured original pillar array. value of r_{def} is used that of nano-texture.

- **Deformed structure**

$$\cos\theta^* = r_{def} \cdot f_{def} \cdot \cos\theta_Y + f_{def} - 1 = 151.5°$$

CHAPTER 7

REFERENCES

1 J. Seo, S. K. Lee, J. Lee, J. S. Lee, H. Kwon, S. W. Cho, J. H. Ahn and T. Lee, *Sci Rep-Uk*, **2015**, *5*.

2 C. J. Huang, W. F. Fang, M. S. Ke, H. Y. E. Chou and J. T. Yang, *Lab Chip*, **2014**, *14*, 2057-2062.

3 Y. Zhang, S. Park, K. Liu, J. Tsuan, S. Yang and T. H. Wang, *Lab Chip*, **2011**, *11*, 398-406.

4 H. H. Shen, S. K. Fan, C. J. Kim and D. J. Yao, *Microfluid Nanofluid*, **2014**, *16*, 965-987.

5 N. Vergauwe, D. Witters, F. Ceyssens, S. Vermeir, B. Verbruggen, R. Puers and J. Lammertyn, *J Micromech Microeng*, **2011**, *21*.

6 V. N. Luk, G. C. H. Mo and A. R. Wheeler, *Langmuir*, **2008**, *24*, 6382-6389.

7 J. Y. Yoon and R. L. Garrell, *Anal Chem*, **2003**, *75*, 5097-5102.

8 R. B. Fair, *Microfluid Nanofluid*, **2007**, *3*, 245-281.

9 J. L. Lin, G. B. Lee, Y. H. Chang and K. Y. Lien, *Langmuir*, **2006**, *22*, 484-489.

10 A. A. Darhuber, J. P. Valentino, S. M. Troian and S. Wagner, *J Microelectromech S*, **2003**, *12*, 873-879.

11 S. Ouenzerfi and S. Harmand, *Langmuir*, **2016**, *32*, 2378-2388.

12 S. Mettu and M. K. Chaudhury, *Langmuir*, **2008**, *24*, 10833-10837.

13 Y. P. Hou, B. L. Xue, S. Guan, S. L. Feng, Z. Geng, X. Sui, J. H. Lu, L. C. Gao and L. Jiang, *Npg Asia Mater*, **2013**, *5*.

14 S. Feng, S. J. Wang, Y. H. Tao, W. F. Shang, S. Y. Deng, Y. M. Zheng and Y. P. Hou, *Sci Rep-Uk*, **2015**, *5*.

15 S. C. Hernandez, C. J. C. Bennett, C. E. Junkermeier, S. D. Tsoi, F. J. Bezares, R. Stine, J. T. Robinson, E. H. Lock, D. R. Boris, B. D. Pate, J. D. Caldwell, T. L. Reinecke, P. E. Sheehan and S. G. Walton, *Acs Nano*, **2013**, *7*, 4746-4755.

16 H. Bai, X. L. Tian, Y. M. Zheng, J. Ju, Y. Zhao and L. Jiang, *Adv Mater*, **2010**, *22*, 5521-5525.

17 J. T. Yang, Z. H. Yang, C. Y. Chen and D. J. Yao, *Langmuir*, **2008**, *24*, 9889-9897.

18 J. T. Yang, J. C. Chen, K. J. Huang and J. A. Yeh, *J Microelectromech S*, **2006**, *15*, 697-707.

19 A. Shastry, M. J. Case and K. F. Bohringer, *Langmuir*, **2006**, *22*, 6161-6167.

20 J. Wu, J. Xia, W. Lei and B. P. Wang, *Sci Rep-Uk*, **2013**, *3*.

21 E. Pierce, F. J. Carmona, and A. Amirfzli, Colloids Surf A, **2008**, *323, 73-82.*

22 D. Y. Kwok, R. Wu, A. Li, A. W. Neumann, Adhes, Sci, Technol, **2000**, *14*, 719-743.

23 H. B. Eral, D. J. C. M. ‘t Mannetje, J. M. Oh, Colloid Polym Sci, **2013**, *291*, 247-260.

24 B. Bhushan, Y. C. Jung and K. Koch, *Philos T R Soc A*, **2009**, *367*, 1631-1672.

25 H. Mertaniemi, V. Jokinen, L. Sainiemi, S. Franssila, A. Marmur, O. Ikkala and R. H. A. Ras, *Adv Mater*, **2011**, *23*, 2911-+.

26 H. Hu, V. V. Swaminathan, M. R. Z. Farahani, G. Mensing, J. Yeom, M. A. Shannon and L. K. Zhu, *J Micromech Microeng*, **2014**, *24*.

27 R. Li, A. Alizadeh and W. Shang, *Phys Rev E*, **2010**, *82*.

28 T. Xie, *Polymer*, **2011**, *52*, 4985-5000.

29 T. Xie and I. A. Rousseau, *Polymer*, **2009**, *50*, 1852-1856.

30 K. Takashima, K. Sugitani, N. Morimoto, S. Sakaguchi, T. Noritsugu and T. Mukai, *Smart Mater Struct*, **2014**, *23*.

31 S. S. M. S. A. Firouzeh, A. Billard, and J. Paik,, *in Proc. IEEE Int. Conf. Robot. Autom. (ICRA)*, **2015**, 2536-2543.

32 W. Small, P. R. Buckley, T. S. Wilson, W. J. Benett, J. Hartman, D. Saloner and D. J. Maitland, *Ieee T Bio-Med Eng*, **2007**, *54*, 1157-1160.

33 A. Lendlein and R. Langer, *Science*, **2002**, *296*, 1673-1676.

34 J. D. Eisenhaure, S. I. Rhee, A. M. Al-Okaily, A. Carlson, P. M. Ferreira and S. Kim, *J Microelectromech S*, **2014**, *23*, 1012-1014.

35 J. D. Eisenhaure, T. Xie, S. Varghese and S. Kim, *Acs Appl Mater Inter*, **2013**, *5*, 7714-7717.

36 J. Eisenhaure and S. Kim, *Polymers-Basel*, **2014**, *6*, 2274-2286.

37 J. Kunzelman, B. R. Crenshaw and C. Weder, *J Mater Chem*, **2007**, *17*, 2989-2991.

38 H. S. Luo, Z. W. Li, G. B. Yi, Y. J. Wang, X. H. Zu, H. Wang, H. L. Huang and Z. F. Liang, *Mater Lett*, **2015**, *140*, 71-74.

39 C. M. Chen and S. Yang, *Adv Mater*, **2014**, *26*, 1283-1288.

40 C. M. Chen, C. L. Chiang and S. Yang, *Langmuir*, **2015**, *31*, 9523-9526.

41 Y. W. Zheng, J. Li, E. Lee and S. Yang, *Rsc Adv*, **2015**, *5*, 30495-30499.

42 G. D. Bixler, A. Theiss, B. Bhushan and S. C. Lee, *J Colloid Interf Sci*, **2014**, *419*, 114-133.

43 M. L. Carman, T. G. Estes, A. W. Feinberg, J. F. Schumacher, W. Wilkerson, L. H. Wilson, M. E. Callow, J. A. Callow and A. B. Brennan, *Biofouling*, **2006**, *22*, 11-21.

44 Z. D. Xu, Y. Yao, E. P. Brueckner, L. F. Li, J. Jiang, R. G. Nuzzo and G. L. Liu, *Nanotechnology*, **2014**, *25*.

45 T. Z. B. Kobrin, M.T. Grimes, K. Chong, M. Wanebo, J. Chinn, R. Nowak, *J. Phys. Conf. Ser.*, **2006**, *34*, 454-457.

46 C. Lee, Y. Nam, H. Lastakowski, J. I. Hur, S. Shin, A. L. Biance, C. Pirat, C. J. Kim and C. Ybert, *Soft Matter*, **2015**, *11*, 4592-4599.

47 A. Marmur, *Langmuir*, **2003**, *19*, 8343-8348.

48 S. Adera, R. Raj, R. Enright and E. N. Wang, *Nat Commun*, **2013**, *4*.

49 G. M. Liu, L. Fu, A. V. Rode and V. S. J. Craig, *Langmuir*, **2011**, *27*, 2595-2600.

50 D. A. del Cerro, A. G. Marin, G. R. B. E. Romer, B. Pathiraj, D. Lohse and A. J. H. in't Veld, *Langmuir*, **2012**, *28*, 15106-15110.